

# A Hermite WENO-based limiter for discontinuous Galerkin method on unstructured grids

Hong Luo <sup>a,\*</sup>, Joseph D. Baum <sup>a</sup>, Rainald Löhner <sup>b</sup>

<sup>a</sup> Center for Applied Computational Sciences, Science Applications International Corporation, 1710 SAIC Drive, MS 2-6-9, McLean, VA 22102, USA

<sup>b</sup> School of Computational Sciences, George Mason University, Fairfax, VA 22030, USA

Received 11 September 2006; received in revised form 20 December 2006; accepted 21 December 2006  
Available online 10 January 2007

## Abstract

A weighted essentially non-oscillatory reconstruction scheme based on Hermite polynomials is developed and applied as a limiter for the discontinuous Galerkin finite element method on unstructured grids. The solution polynomials are reconstructed using a WENO scheme by taking advantage of handily available and yet valuable information, namely the derivatives, in the context of the discontinuous Galerkin method. The stencils used in the reconstruction involve only the van Neumann neighborhood and are compact and consistent with the DG method. The developed HWENO limiter is implemented and used in a discontinuous Galerkin method to compute a variety of both steady-state and time-accurate compressible flow problems on unstructured grids. Numerical experiments for a wide range of flow conditions in both 2D and 3D configurations are presented to demonstrate the accuracy, effectiveness, and robustness of the designed HWENO limiter for the DG methods.

© 2007 Elsevier Inc. All rights reserved.

*Keywords:* Discontinuous Galerkin methods; WENO; Compressible flows; Unstructured grids; Slope limiters

## 1. Introduction

The discontinuous Galerkin methods [1,2] (DGM) have recently become popular for the solution of systems of conservation laws to arbitrary order of accuracy. The discontinuous Galerkin methods combine two advantageous features commonly associated to finite element and finite volume methods. As in classical finite element methods, accuracy is obtained by means of high-order polynomial approximation within an element rather than by wide stencils as in the case of finite volume methods. The physics of wave propagation is, however, accounted for by solving the Riemann problems that arise from the discontinuous representation of the solution at element interfaces. In this respect, the methods are therefore similar to finite volume methods. In fact, the basic cell-centered finite volume scheme exactly corresponds to the DG(0) method, i.e., to the

\* Corresponding author. Tel.: +1 703 676 5957; fax: +1 703 676 5323.  
E-mail address: [hong.luo@saic.com](mailto:hong.luo@saic.com) (H. Luo).

discontinuous Galerkin method using piecewise constant polynomials. Consequently, the DG( $p$ ) method with  $p > 0$  can be regarded as the natural extension of finite volume methods to higher-order methods. The discontinuous Galerkin methods have many distinguished features: (1) The methods are well suited for complex geometries since they can be applied on unstructured grids. In addition, the methods can also handle non-conforming elements, where the grids are allowed to have hanging nodes. (2) The methods are compact, as each element is independent. Since the elements are discontinuous, and the inter-element communications are minimal (elements only communicate with von Neumann neighbors regardless of the order of accuracy of the scheme), they are highly parallelizable. The compactness also allows for structured and simplified coding for the methods. (3) They can easily handle adaptive strategies, since refining or coarsening a grid can be achieved without considering the continuity restriction commonly associated with the conforming elements. The methods allow easy implementation of  $hp$ -refinement, for example, the order of accuracy, or shape, can vary from element to element. (4) They have several useful mathematical properties with respect to conservation, stability, and convergence.

However, the discontinuous Galerkin methods have a number of their own weaknesses. In particular, how to effectively control spurious oscillations in the presence of strong discontinuities remains one of unresolved issues in the DG methods. Like any higher-order schemes ( $>1$ ), the discontinuous Galerkin methods will suffer from non-physical oscillations in the vicinity of discontinuities that exist in problems governed by hyperbolic conservation laws. Two common approaches to address this issue are a discontinuity capturing and an appropriate slope limiter. The former adds explicitly consistent artificial viscosity terms to the discontinuous Galerkin discretization. The main disadvantage of this approach is that it usually requires some user-defined parameters, which can be both mesh and problem dependent. Classical techniques of slope limiting are not directly applicable for high-order DGM because of the presence of volume terms in the formulation. Therefore, the slope limiter is not integrated in the computation of the residual, but effectively acts as a post-processing filter. Many slope limiters used in the finite volume method (FVM) can then be used or modified to meet the needs of the DGM. Unfortunately, the use of the limiter will reduce the order of accuracy to first order in the presence of discontinuities. Furthermore, the active limiters in the smooth extrema will pollute the solution in the flow field and ultimately destroy the higher-order accuracy of DGM [3]. Indeed, the limiters used in TVD/MUSCL finite volume methods are less robust than the strategies of essential non-oscillatory (ENO) and weighted ENO (WENO) finite volume methods. The ENO schemes were initially introduced by Harten et al. [4] in which oscillations up to the order of the truncation error are allowed to overcome the drawbacks and limitations of limiter-based schemes. ENO schemes avoid interpolation across high-gradient regions through biasing of the reconstruction. This biasing is achieved by reconstructing the solution on several stencils at each location and selecting the reconstruction which is in some sense the smoothest. This allows ENO schemes to retain higher-order accuracy near high-gradient regions. However, the selection process can lead to convergence problems and loss of accuracy in regions with smooth solution variations. To counter these problems, the so-called weighted ENO scheme introduced by Liu et al. [5] is designed to present better convergence rate for steady state problems, better smoothing for the flux vectors, and better accuracy using the same stencils than the ENO scheme. WENO scheme uses a suitably weighted combination of all reconstructions rather than just the one which is judged to be the smoothest. The weighting is designed to favor the smooth reconstruction in the sense that its weight is small, if the oscillation of a reconstructed polynomial is high and its weight is order of one, if a reconstructed polynomial has low oscillation. Qiu and Shu initiated the use of WENO scheme as limiters for the DG method [6] for solving 1D and 2D Euler equations on structured grids. Later on, they constructed a class of WENO schemes based on Hermite polynomials, termed as HWENO (Hermite WENO) schemes and applied this HWENO as limiters for the DG methods [7,8]. The main difference between HWENO and WENO schemes is that the former has a more compact stencil than the latter for the same order of accuracy.

Unfortunately, implementation of both ENO and WENO schemes is fairly complicated on arbitrary meshes, especially in 3D. In fact, there are very few results obtained using ENO/WENO on unstructured grids in 3D especially for higher-order reconstruction. Harten and Chakravarthy [9], Abgrall [10], and Sonar [11] presented the first implementation of ENO schemes on unstructured triangular grids. Implementations of WENO methods on unstructured triangular grids were also presented by Friedrich [12] and Hu and Shu [13].

In the present work, a WENO reconstruction scheme based on the Hermite polynomials is presented and used as a non-linear limiter for a discontinuous Galerkin method to solve the compressible Euler equations on unstructured grids. The new reconstruction scheme makes use of the invaluable information, namely derivatives that are handily available in the context of the discontinuous Galerkin method, thus making the implementation of WENO schemes straightforward on unstructured grids in both 2D and 3D. Only the van Neumann neighborhood is required for the construction of stencils, regardless of the order of solution polynomials to be reconstructed. The resulting HWENO reconstruction keeps full conservation of mass, momentum, and energy, is uniformly accurate with no overshoots and undershoots, is easy to implement on arbitrary meshes, has good convergence properties, and is computationally efficient. This HWENO limiter is implemented and used in a discontinuous Galerkin method to compute a variety of both steady-state and time-accurate compressible flow problems on unstructured grids. Numerical experiments for a wide range of flow conditions in both 2D and 3D configurations are presented to demonstrate the accuracy, effectiveness, and robustness of the designed HWENO limiter. The remainder of this paper is structured as follows. The governing equations are listed in Section 2. The underlying discontinuous Galerkin method is presented in Section 3. The construction and implementation of the limiter based on the HWENO scheme are described in detail in Section 4. Extensive numerical experiments are reported in Section 5. Concluding remarks are given in Section 6.

## 2. Governing equations

The Euler equations governing unsteady compressible inviscid flows can be expressed in conservative form as

$$\frac{\partial \mathbf{U}(\mathbf{x}, t)}{\partial t} + \frac{\partial \mathbf{F}_j(\mathbf{U}(\mathbf{x}, t))}{\partial x_j} = 0, \quad (2.1)$$

where the conservative state vector  $\mathbf{U}$  and the inviscid flux vectors  $\mathbf{F}$  are defined by

$$\mathbf{U} = \begin{pmatrix} \rho \\ \rho u_i \\ \rho e \end{pmatrix}, \quad \mathbf{F} = \begin{pmatrix} \rho u_j \\ \rho u_i u_j + p \delta_{ij} \\ u_j(\rho e + p) \end{pmatrix}, \quad (2.2)$$

where the summation convention has been used and  $\rho$ ,  $p$ , and  $e$  denote the density, pressure, and specific total energy of the fluid, respectively, and  $u_i$  is the velocity of the flow in the coordinate direction  $x_i$ . This set of equations is completed by the addition of the equation of state

$$p = (\gamma - 1)\rho \left( e - \frac{1}{2} u_j u_j \right), \quad (2.3)$$

which is valid for perfect gas, where  $\gamma$  is the ratio of the specific heats.

## 3. Discontinuous Galerkin method

### 3.1. Discontinuous Galerkin spatial discretization

To formulate the discontinuous Galerkin method, we first introduce the following weak formulation of Eq. (2.1), which is obtained by multiplying Eq. (2.1) by a test function  $\mathbf{W}$ , integrating over the domain  $\Omega$ , and performing an integration by parts:

$$\int_{\Omega} \frac{\partial \mathbf{U}}{\partial t} \mathbf{W} \, d\Omega + \int_{\Gamma} \mathbf{F}_j \mathbf{n}_j \mathbf{W} \, d\Gamma - \int_{\Omega} \mathbf{F}_j \frac{\partial \mathbf{W}}{\partial x_j} \, d\Omega \quad \forall \mathbf{W}, \quad (3.1)$$

where  $\Gamma (= \partial\Omega)$  denotes the boundary of  $\Omega$ , and  $\mathbf{n}_j$  the unit outward normal vector to the boundary.

Assuming that  $\Omega_h$  is a classical triangulation of  $\Omega$  where the domain  $\Omega$  is subdivided into a collection of non-overlapping elements  $\Omega_e$ , triangles in 2D and tetrahedra in 3D, the following semi-discrete form of Eq. (3.1) is obtained by applying Eq. (3.1) on each element  $\Omega_e$

$$\frac{d}{dt} \int_{\Omega_e} \mathbf{U}_h \mathbf{W}_h \, d\Omega + \int_{\Gamma_e} \mathbf{F}_j(\mathbf{U}_h) \mathbf{n}_j \mathbf{W}_h \, d\Gamma - \int_{\Omega_e} \mathbf{F}_j(\mathbf{U}_h) \frac{\partial \mathbf{W}_h}{\partial x_j} \, d\Omega \quad \forall \mathbf{W}_h, \tag{3.2}$$

where  $\Gamma_e (= \partial\Omega_e)$  denotes the boundary of  $\Omega_e$ , and  $\mathbf{U}_h$  and  $\mathbf{W}_h$  represent the finite element approximations to the analytical solution  $\mathbf{U}$  and the test function  $\mathbf{W}$ , respectively. Assume that the approximate solution and test function to be piece-wise polynomials in each element, then  $\mathbf{U}_h$  and  $\mathbf{W}_h$  can be expressed as

$$\mathbf{U}_h(\mathbf{x}, t) = \sum_{m=1}^N \mathbf{U}_m(t) B_m^p(\mathbf{x}), \quad \mathbf{W}_h(\mathbf{x}) = \sum_{m=1}^N \mathbf{W}_m B_m^p(\mathbf{x}), \tag{3.3}$$

where  $B_m^p(\mathbf{x})$ ,  $1 \leq m \leq N$  is the basis function of the polynomials of degree  $p$ . The dimension of the polynomial space,  $N = N(p, d)$  depends on the degree of the polynomials of the expansion  $p$ , and the number of spatial dimensions  $d$ , as

$$N = \frac{(p+1)(p+2) \cdots (p+d)}{d!} \quad \text{for } d = 1, 2, 3. \tag{3.4}$$

Eq. (3.2) must be satisfied for any test function  $\mathbf{W}_h$ . Since  $B_n^p$  is the basis for  $\mathbf{W}_h$ , Eq. (3.2) is, therefore, equivalent to the following system of  $N$  equations

$$\frac{d\mathbf{U}_m}{dt} \int_{\Omega_e} B_m^p B_n^p \, d\Omega + \int_{\Gamma_e} \mathbf{F}_j(\mathbf{U}_h) \mathbf{n}_j B_n^p \, d\Gamma - \int_{\Omega_e} \mathbf{F}_j(\mathbf{U}_h) \frac{\partial B_n^p}{\partial x_j} \, d\Omega = 0, \quad 1 \leq n \leq N, \tag{3.5}$$

where  $\mathbf{U}_h$  is replaced with Eq. (3.3). Since the numerical solution  $\mathbf{U}_h$  is discontinuous between element interfaces, the interface fluxes are not uniquely defined. The flux function  $\mathbf{F}_j(\mathbf{U}_h) \mathbf{n}_j$  appearing in the second term of Eq. (3.5) is replaced by a numerical Riemann flux function  $\mathbf{H}(\mathbf{U}_h^L, \mathbf{U}_h^R, \mathbf{n})$ , where  $\mathbf{U}_h^L$  and  $\mathbf{U}_h^R$  are the conservative state vector at the left and right side of the element boundary. In order to guarantee consistency and conservation,  $\mathbf{H}(\mathbf{U}^L, \mathbf{U}^R, \mathbf{n})$  is required to satisfy

$$\mathbf{H}(\mathbf{U}, \mathbf{U}, \mathbf{n}) = \mathbf{F}_j(\mathbf{U}) \mathbf{n}_j, \quad \mathbf{H}(\mathbf{U}, \mathbf{V}, \mathbf{n}) = -\mathbf{H}(\mathbf{V}, \mathbf{U}, \mathbf{n}). \tag{3.6}$$

This scheme is called discontinuous Galerkin method of degree  $p$ , or in short notation ‘‘DG( $p$ ) method’’. Note that discontinuous Galerkin formulations are very similar to finite volume schemes, especially in their use of numerical fluxes. Indeed, the classical first-order cell-centered finite volume scheme exactly corresponds to the DG(0) method, i.e., to the discontinuous Galerkin method using piece-wise constant polynomials. Consequently, the DG( $p$ ) methods with  $p > 0$  can be regarded as a ‘‘natural’’ generalization of finite volume methods to higher-order methods. By simply increasing the degree  $p$  of the polynomials, DG methods of corresponding higher orders are obtained.

In the present work, the Riemann flux function is approximated using the HLLC approximate Riemann solver [14], which has been successfully used to compute compressible viscous and turbulent flows on both structured grids [15] and unstructured grids [16]. This HLLC scheme is found to have the following properties: (1) exact preservation of isolated contact and shear waves, (2) positivity-preserving of scalar quantity, (3) enforcement of entropy condition. In addition, the implementation of HLLC Riemann solver is easier and the computational cost is lower compared with other available Riemann solvers.

The domain and boundary integrals in Eq. (3.5) are calculated using  $2p$  and  $2p + 1$  order accurate Gauss quadrature formulas, respectively. The number of quadrature points necessary for a given order depends on the quadrature rule used. In the case of linear, quadratic, and cubic shape function, the domain integrals are evaluated using 3, 6, and 12 points respectively, and the boundary integrals are evaluated using two, three, and four points, respectively, for 2D. In 3D, integration over the elements for P1 and P2 approximation is performed using 4 and 11 quadrature points, respectively, and integration over the element boundaries for P0, P1, and P2 is performed using one, four, and seven quadrature points, respectively.

By assembling together all the elemental contributions, a system of ordinary differential equations governing the evolution in time of the discrete solution can be written as

$$M \frac{d\mathbf{U}}{dt} = \mathbf{R}(\mathbf{U}), \tag{3.7}$$

where  $M$  denotes the mass matrix,  $\mathbf{U}$  is the global vector of the degrees of freedom, and  $\mathbf{R}(\mathbf{U})$  is the residual vector. Since the shape functions  $B^p|_{\Omega_e}$  are nonzero within element  $\Omega_e$  only, the mass matrix  $M$  has a block

diagonal structure that couples the  $N$  degrees of freedom of each component of the unknown vector only within  $\Omega_e$ . As a result, the inverse of the mass matrix  $M$  can be easily computed by hand considering one element at a time in advance.

### 3.2. Time integration

The semi-discrete system can be integrated in time using explicit methods. For example, the following explicit three-stage third-order TVD Runge–Kutta scheme [2]

$$\mathbf{U}^{(1)} = \mathbf{U}^n + \Delta t M^{-1} \mathbf{R}(\mathbf{U}^n), \quad (3.8)$$

$$\mathbf{U}^{(2)} = \frac{3}{4} \mathbf{U}^n + \frac{1}{4} [\mathbf{U}^{(1)} + \Delta t M^{-1} \mathbf{R}(\mathbf{U}^{(1)})], \quad (3.9)$$

$$\mathbf{U}^{n+1} = \frac{1}{3} \mathbf{U}^n + \frac{2}{3} [\mathbf{U}^{(2)} + \Delta t M^{-1} \mathbf{R}(\mathbf{U}^{(2)})], \quad (3.10)$$

is widely used to advance the solution in time. This method is linearly stable for a Courant number less than or equal to  $1/(2p + 1)$ . The inefficiency of the explicit method due to this rather restrictive CFL condition motivates us to develop the  $p$ -multigrid method [17,18] to accelerate the convergence of the Euler equations to a steady state solution. Unlike the traditional  $p$ -multigrid methods where the same time integration scheme is used on all approximation levels, this  $p$ -multigrid method uses the above multi-stage Runge–Kutta scheme as the iterative smoother on the higher level approximations ( $p > 0$ ), and a matrix-free implicit SGS method as the iterative smoother on the lowest level approximation ( $p = 0$ ). As a result, this  $p$ -multigrid method has two remarkable features: (1) Low memory requirements. The implicit smoothing is only used on the lowest level  $P_0$ , where the storage requirement is not as demanding as on the higher level; (2) Natural extension to flows with discontinuities such as shock waves and contact discontinuities. A monotonic limiting procedure required to eliminate spurious oscillations of high-order approximations in the vicinity of discontinuities can be easily implemented as a post-processing filter (smoothing) in an explicit method, but not in an implicit method. This  $p$ -multigrid is found to be orders of magnitude faster than its explicit counterpart without significant increase in memory for computing steady-state flow problems.

## 4. Hermite WENO reconstruction

The DG method described above will produce non-physical oscillations and even nonlinear instability for flows with strong discontinuities. A common solution to this problem is to use a slope limiter. Unfortunately, DGM are very sensitive to the treatment and implementation of the slope limiters [3]. Slope limiters frequently identify regions near smooth extrema as requiring limiting, and this typically results in a reduction of the optimal high-order convergence rate. For aerodynamic applications, the active limiters close to the smooth extrema such as a leading edge of an airfoil will contaminate the solution in the flow field and ultimately destroy the high-order accuracy of the DG solution. Alternatively, the ENO/WENO methodology can be used as a limiter for the discontinuous Galerkin methods, as it is more robust than the slope limiter methodology, and can achieve both uniform high-order accuracy and a sharp, ENO shock transitions. This is accomplished by replacing the solution polynomials with reconstructed polynomials, which maintain the original cell averages of flow variables (full conservation of mass, momentum, and total energy), have the same high-order of accuracy as before in the regions where the solution is smooth, but oscillation-free behavior in the vicinity of discontinuities. A typical WENO cell-centered finite volume reconstruction scheme for a function  $u$  consists of the following steps:

1. Identify a number of admissible stencils  $S_1, S_2, \dots, S_m$  for a cell  $\Omega_e$  consisting of the neighboring cells, such that the cell itself  $\Omega_e$  belongs to each stencil. Note that a stencil can be thought of as a set of cells that can be used to obtain a polynomial reconstruction.
2. Reconstruct the function  $u$  for each stencil  $S_i$  by a polynomial  $P_i$  based on the mean values of the function  $u$  on each cell in the stencil  $S_i$

3. Compute an oscillation indicator  $o_i$  for each reconstructed polynomial  $P_i$ .
4. Calculate weights  $w_i$  for each  $P_i$  using oscillation indicator such that the sum of  $w_i$  is one.
5. Find the reconstruction polynomial  $p$  as the weighted sum of the  $P_i$ ,  $p = \sum_{i=1}^m w_i P_i$ .

Obviously, the selection of stencils plays a vitally critical role to the success of the reconstruction algorithm. One has to take into account some of more or less contradictory arguments: On the one hand, the stencils should have a small diameter and are well centered with respect to  $\Omega_e$  to obtain high accuracy and stability in smooth regions. The number of stencils should be small to reduce the computational cost; On the other hand, ENO methods are based on the idea that in case of non-smooth regions one-sided stencils are chosen to avoid interpolation across discontinuities. The number of stencils should be large enough to avoid any oscillation in the solutions and keep the scheme stable.

For the construction of a polynomial of degree  $p$ , the dimension of the polynomial space,  $N = N(p, d)$  depends on the degree of the polynomials of the expansion  $p$ , and the number of spatial dimensions  $d$ , determined by Eq. (3.4). One must have 3, 6, and 10 cells in 2D and 4, 10, and 20 cells in 3D for the construction of a linear, quadratic, and cubic Lagrange polynomial, respectively. Undoubtedly, it is an overwhelmingly challenging, if not practically impossible, task to judiciously choose a set of admissible and proper stencils that have such a large number of cells on unstructured grids especially for higher-order polynomials and higher dimensions. This explains why the application of higher-order ENO/WENO methods hardly exist on unstructured grids, in spite of their tremendous success on structured grids and their superior performance over the MUSCL/TVD methods.

However, the number of cells needed for a polynomial reconstruction can be significantly reduced, if a Hermite polynomial is used instead of a Lagrange one. This is only possible, if the first derivatives of the function to be reconstructed are known on the cells. Fortunately, this is exactly the case for the discontinuous Galerkin methods where the derivatives are handily available on each cell. Here, we confine ourself to the case of Hermite WENO reconstruction for a linear polynomial  $P_1$ . However, the idea can be used for the reconstruction of higher-order polynomials as well, though the second and higher derivatives need to be taken into consideration, and will be reported in a following paper. The reconstruction process of the HWENO schemes for the DG methods is based on the approximation of mean and first derivative values of the flow variables for each cell in the mesh. The stencils are only chosen in a von Neumann neighborhood in order to be compact and consistent with the DG method. More precisely, for cell  $\Omega_e$ , the following three stencils ( $\Omega_e\Omega_a\Omega_b$ ,  $\Omega_e\Omega_b\Omega_c$ ,  $\Omega_e\Omega_c\Omega_a$ ), shown in Fig. 1, are chosen to construct a Lagrange polynomial such that

$$\frac{1}{|\Omega_e|} \int_{\Omega_e} P_1 \, d\Omega = u_e,$$

$$\frac{1}{|\Omega_j|} \int_{\Omega_j} P_1 \, d\Omega = u_j, \quad \frac{1}{|\Omega_k|} \int_{\Omega_k} P_1 \, d\Omega = u_k \quad (j, k) = (a, b; b, c; c, a),$$

and the following four stencils ( $\Omega_e\Omega_e$ ,  $\Omega_e\Omega_a$ ,  $\Omega_e\Omega_b$ ,  $\Omega_e\Omega_c$ ) are chosen to construct a Hermite polynomial such that,

$$\frac{1}{|\Omega_e|} \int_{\Omega_e} P_1 \, d\Omega = u_e, \quad \frac{1}{|\Omega_k|} \int_{\Omega_k} \frac{\partial P_1}{\partial x_i} \, d\Omega = \left. \frac{\partial P_1}{\partial x_i} \right|_k \quad (k = e, a, b, c).$$

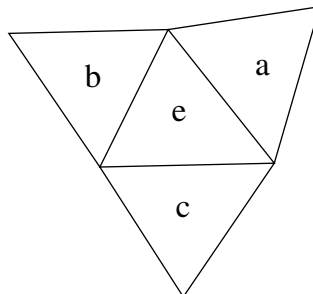


Fig. 1. Neighborhood defined by the von Neumann neighbors of the cell  $\Omega_e$  used for HWENO reconstruction.



The present choice is unique, symmetric, compact, and most importantly consistent with the underlying DG methods, as only van Neumann neighbors are involved in the reconstruction. This means that no additional data structure is required and the compactness of the DG methods is maintained. Note that the number of the resulting stencils, except the solution polynomial itself, is six in 2D, exactly the same as the ones used in Refs. [11,12], and eight in 3D. Since the first derivatives are handily available in the DG method, there is no need to actually reconstruct the four Hermite polynomials in 2D (five in 3D) and only the three Lagrange polynomials in 2D (four in 3D) need to be reconstructed, representing a big saving in computing costs.

After the polynomial reconstruction is performed for each cell, an oscillation indicator is sought to assess the smoothness of  $P$ . Following the results presented in the literature [12], the oscillation indicator used in the present work is the one proposed by Jiang and Shu [19], which was later modified by Friedrich [12]. The oscillation indicator for the reconstructed polynomial  $P_i$  can be defined as

$$o_i = \left[ \int_{\Omega_i} h^{-2} \left( \frac{\partial P_i}{\partial x_k} \right)^2 d\Omega \right]^{\frac{1}{2}},$$

where  $h = \text{mes}(\Omega_e)$  is the mesh width.

Unlike the ENO schemes, the WENO schemes use all the computed polynomials. These polynomials are added together through the use of weights which are determined for each one of the polynomials as proportional to its respective oscillation indicator. The main idea in the WENO reconstruction is to attribute the computed weights for each polynomial with the aim of reconstructing a new polynomial as  $P = \sum_{i=1}^m w_i P_i$ . The weights are computed as

$$w_i = \frac{(\epsilon + o_i(P_i))^{-\gamma}}{\sum_{k=1}^m (\epsilon + o_i(P_k))^{-\gamma}},$$

where  $\gamma$  is a positive number.

Note that this type of limiting is fundamentally different from the one used in TVD schemes. Reconstruction scheme based on the WENO limiting weights gradients obtained from neighboring stencils in order to continuously eliminate these which cause oscillations. From the perspective of both computational cost and numerical accuracy, the above HWENO limiting should only be used in the regions where strong discontinuities exist. This can be accomplished using the so-called discontinuity detectors, which are helpful to distinguish regions where solutions are smooth and discontinuous. The beauty of this HWENO limiter is that in case that the limiting is mistakenly applied in the smooth cells, the uniform high-order accuracy can still be maintained, unlike the slope limiters, which, when applied near smooth extrema, will have a profoundly adverse impact on solution in the smooth region, leading the loss of the original high-order accuracy. This remarkable feature of the HWENO limiter in turn alleviates the burden on the discontinuity detectors, as no discontinuity detectors can really either in theory or in practice make a distinction between a stagnation point and a shock wave, as flow gradients near the stagnation point are even larger than the ones near the shock wave in some cases. All numerical experiments to be presented in the next section are performed by applying the limiters everywhere in an effort to ensure that the computational results are not affected by a shock detector, and to demonstrate the superior properties of the designed HWENO limiter.

## 5. Numerical examples

All computations are performed on a Dell Precision M70 laptop computer with 2GBytes memory running the Suse 10.0 Linux operating system. The explicit three-stage third-order TVD Runge–Kutta scheme is used for unsteady flow computations and the  $p$ -multigrid for steady-state flow problems. For steady-state solutions, the relative  $L_2$  norm of the density residual is taken as a criterion to test convergence history. All calculations are started with uniform flow. An elaborate and well-tested finite volume code [16,20] is used as a reference to quantitatively compare the accuracy of the DG method for steady-state solutions, although it is not our objective to compare the performance of FV and DG methods in terms of computational efficiency and numerical accuracy. Relatively coarse meshes are purposely used in all test cases in order to demonstrate higher accuracy of the DG methods as compared with the FV methods. To plot a flow variable on the surface of the solid body

in 2D, its values at two end points of the face of a triangle on the solid body are drawn using a line. This is the most accurate way to represent P1 solution for profile plotting, as the solution is linear on each face (triangle) and multiple values exist for a vertex due to the discontinuous representation of DG solution. For unsteady flow problems, the WENO unstructured grid solutions [13] are used as a reference to qualitatively compare the accuracy of the present DG method.

5.1. Subsonic flows past a circular cylinder

The first example is a well-known test case: subsonic flow past a circular cylinder at a Mach number of  $M_\infty = 0.38$ . This test case is chosen to verify the implementation of HWENO limiter for DG methods and compare the numerical error and orders of accuracy among the FV and DG methods without a limiter and the DG method with a HWENO limiter to assess whether the HWENO limiter will compromise the designed order of accuracy of the original DG method. The four successively refined *o*-type grids used in the computation are shown in Fig. 2, which consists of  $16 \times 5$ ,  $32 \times 9$ ,  $64 \times 17$ , and  $128 \times 33$  points, respectively. The first number refers to the number of points in the circular direction, and the second designates the number of concentric circles in the mesh. The radius of the cylinder is  $r_1 = 0.5$ , the domain is bounded by  $r_{33} = 20$ , and the radii of concentric circles for  $128 \times 33$  mesh are set up as

$$r_i = r_1 \left( 1 + \frac{2\pi}{128} \sum_{j=0}^{i-1} \alpha^j \right), \quad i = 2, \dots, 33,$$

where  $\alpha = 1.1580372$ . The coarser grids are generated by successively un-refining the finest mesh.

Numerical solutions to this problem are computed using FV(P1) and DG(P1) without a limiter and DG(P1) method with a HWENO limiter on these four grids to obtain quantitative measurement of the order of accuracy and discretization errors. The detailed results of this test case are presented in Tables 1a–1c. They show the mesh size, the number of degrees of freedom, the  $L^2$ -error of the solutions, and the order of convergence. In this case, the following entropy production  $\epsilon$  defined as

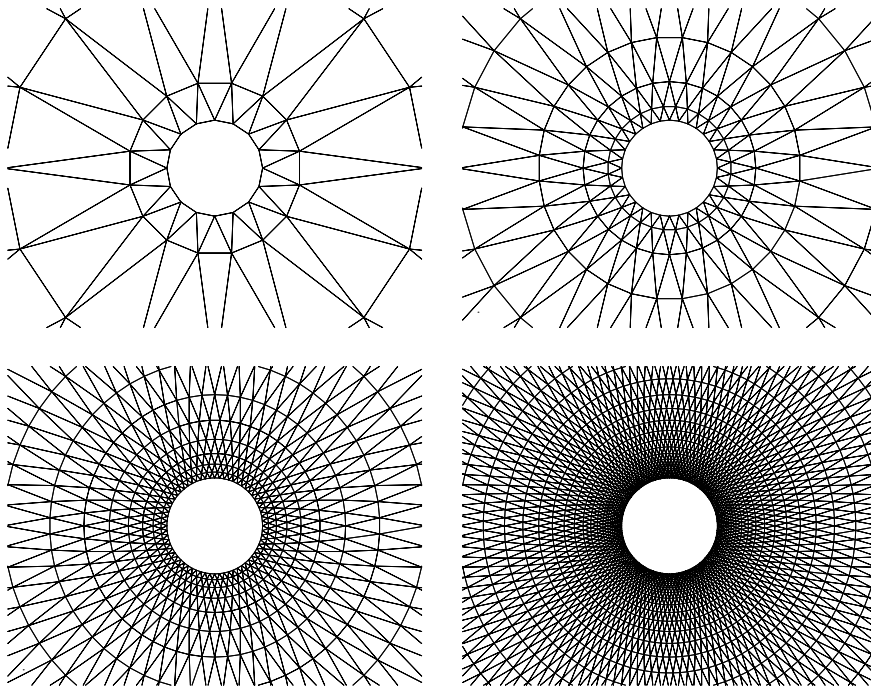


Fig. 2. Sequences of four successively globally refined meshes  $16 \times 5$ ,  $32 \times 9$ ,  $64 \times 17$ ,  $128 \times 33$  for computing subsonic flow past a circular cylinder.



Table 1a  
Subsonic cylinder test case: FV(1) is order of  $O(h^2)$

Mesh	No. DOFs	$L^2$ -error	Order
$16 \times 5$	80	2.37148E-01	–
$32 \times 9$	288	7.76551E-02	1.595
$64 \times 17$	1088	1.36962E-02	2.551
$128 \times 33$	4224	3.54568E-03	1.951

Table 1b  
Subsonic cylinder test case: DG(P1) without a limiter is order of  $O(h^2)$

Mesh	No. DOFs	$L^2$ -error	Order
$16 \times 5$	360	5.68722E-02	–
$32 \times 9$	1536	1.07103E-02	2.443
$64 \times 17$	6144	1.67302E-03	2.688
$128 \times 33$	24,576	2.34369E-04	2.838

Table 1c  
Subsonic cylinder test case: DG(P1) with a HWENO limiter is order of  $O(h^2)$

Mesh	No. DOFs	$L^2$ -error	Order
$16 \times 5$	360	1.19012E-01	–
$32 \times 9$	1536	3.12104E-02	1.958
$64 \times 17$	6144	4.06349E-03	2.952
$128 \times 33$	24,576	5.10387E-04	2.996

$$\epsilon = \frac{S - S_\infty}{S_\infty} = \frac{p}{p_\infty} \left( \frac{\rho_\infty}{\rho} \right)^\gamma - 1,$$

is served as the error measurement, where  $S$  is the entropy. Note that the entropy production serves as a good criterion to measure accuracy of the numerical solutions, since the flow under consideration is isentropic. Fig. 3 provides the details of the spatial accuracy of each method for this numerical experiment. One can see that the solution obtained by FVM method is much more dissipative, as shown on the Mach number contours in the flow field in Fig. 4. This observation becomes especially apparent in Fig. 5, where one compares the entropy production on the surface of cylinder obtained by FV(P1) and DG(P1) without a limiter and DG(P1) with HWENO

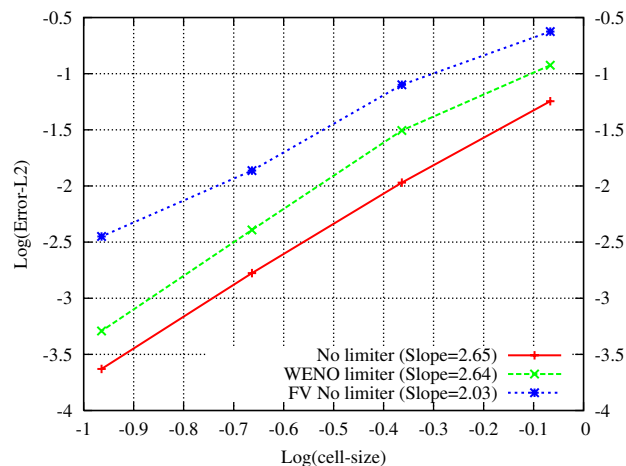


Fig. 3. Results of grid-refinement study for flow past a cylinder obtained by the FV and DG methods without any limiter and the DG method with a WENO limiter.

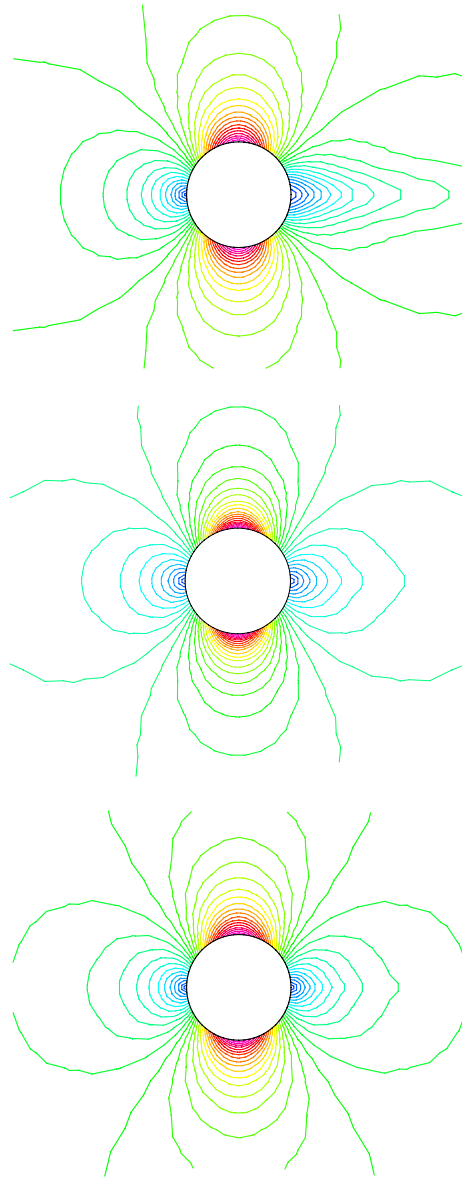


Fig. 4. Computed Mach number contours obtained by the FV(P1) method without a limiter (top), the DG(P1) method with a WENO limiter (middle), and the DG(P1) method without a limiter (bottom) on  $64 \times 17$  mesh for subsonic flow past a circular cylinder at  $M_\infty = 0.38$ .

limiter on the  $64 \times 17$  mesh. The results obtained by the DG method with a HWENO limiter, not as good as those obtained by the DG method without any limiter, indicate that the HWENO limiter does increase slightly the absolute error, although it keeps the designed order of accuracy of the original DG method, a full  $O(h^{p+1})$  order of convergence on smooth solutions. However, even using the HWENO limiter, the DG solution is much more accurate than unlimited FV solution, clearly demonstrating the higher accuracy of the DG method.

### 5.2. Transonic flow past a NACA0012 airfoil

The second example is the transonic flow past a NACA0012 airfoil. The mesh used in the computation is shown in Fig. 6, consisting of 1999 elements, 1048 grid points, and 97 boundary points. The first computation

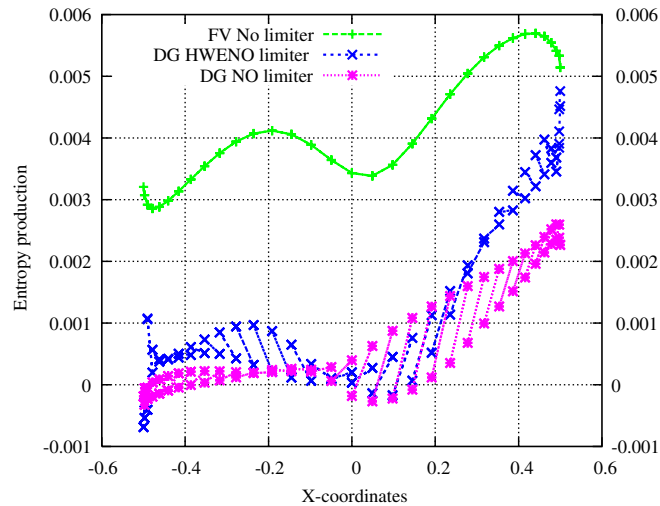


Fig. 5. Comparison of computed entropy production on the surface of the cylinder by the FV(P1) and DG(P1) methods without a limiter and DG(P1) method with a HWENO limiter on  $64 \times 17$  mesh for subsonic flow past a circular cylinder at  $M_\infty = 0.38$ .

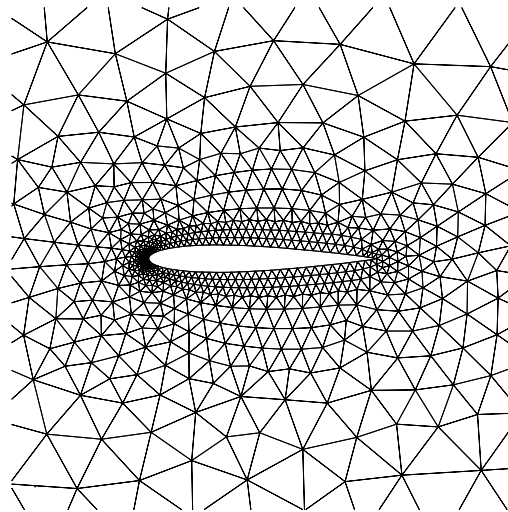


Fig. 6. Unstructured mesh ( $n_{\text{elem}} = 1999$ ,  $n_{\text{poin}} = 1048$ ,  $n_{\text{boun}} = 97$ ) used for computing transonic flow past a NACA0012 airfoil.

is performed at a Mach number of 0.8, and an angle of attack  $1.25^\circ$ , characterized by the existence of a strong shock on the upper surface and a weak shock on the lower surface. This computation is chosen primarily to demonstrate the superior accuracy of second-order DG method over the second finite volume method and assess the performance of the HWENO limiter in terms of solution accuracy and convergence history for flows with shock waves. Fig. 7 shows the computed Mach number contours in the flow field using DG and FV methods without any limiters and DG method with the HWENO limiter, respectively. As expected, the spurious oscillations in the vicinity of shocks do appear in the two unlimited solutions, and HWENO limiter is indeed able to eliminate these oscillations. Note that the finite volume solution is so dissipative that it is unable to resolve the weak shock on the lower surface of the airfoil because of relative coarse mesh used in the computation. The results obtained by DG method appear to be much better than those obtained by its finite volume counterpart, as shown in Figs. 8 and 9, where the pressure coefficient and entropy production on the surface of the airfoil are compared for these three solutions, demonstrating the superior accuracy of the DG method over

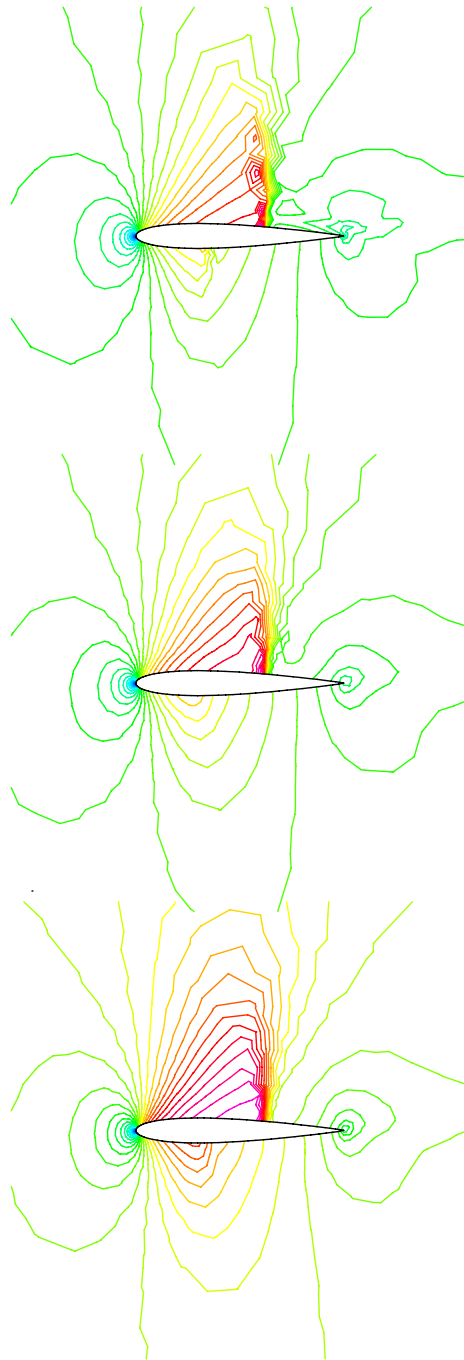


Fig. 7. Computed Mach number contours by the DG method without any limiter (top), the FV method without any limiter (middle), and the DG method with WENO limiter (bottom) for transonic flow past a NACA0012 airfoil at  $M_\infty = 0.8$ ,  $\alpha = 1.25^\circ$ .

the FV method. One can also observe that the use of HWENO limiter does reduce the solution accuracy as witnessed by the increasing level of entropy production in the vicinity of the leading edge, however the magnitude of entropy production generated by the HWENO reconstruction is still much smaller than the one produced by the unlimited second-order finite volume solution, demonstrating the highly accuracy of the HWENO reconstruction scheme. To illustrate the importance of limiters on the DG solution and the accuracy and robustness of the HWENO limiter, one compares the DG solutions obtained using Barth–Jespersen [21]

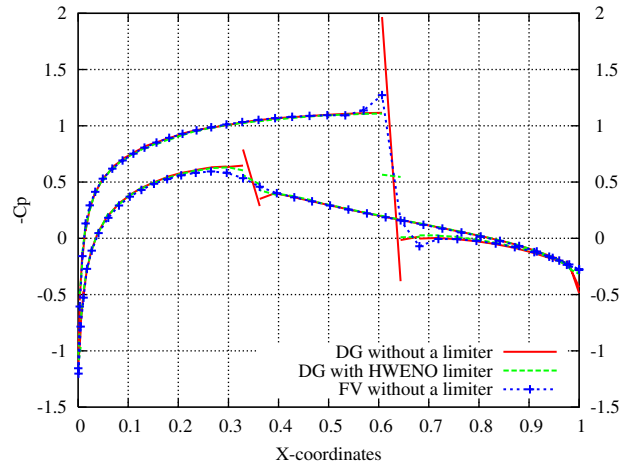


Fig. 8. Comparison of computed pressure coefficient distributions on the surface of airfoil obtained by the DG and FV solution without any limiter, and DG with WENO limiter for transonic flow past a NACA0012 airfoil at  $M_\infty = 0.8$ ,  $\alpha = 1.25^\circ$ .

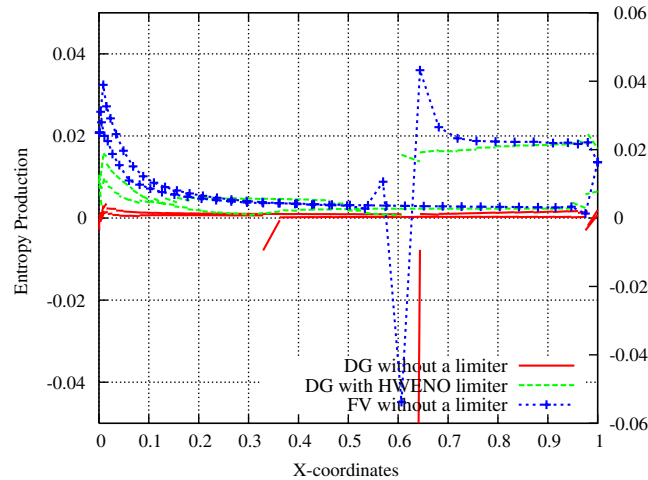


Fig. 9. Comparison of computed entropy production distributions on the surface of airfoil obtained by the DG and FV solution without any limiter, and DG with WENO limiter for transonic flow past a NACA0012 airfoil at  $M_\infty = 0.8$ ,  $\alpha = 1.25^\circ$ .

and HWENO limiters. Figs. 10 and 11 show the pressure coefficient and entropy production on the surface of the airfoil obtained by these two solutions, respectively. As expected, Barth–Jespersen limiter is able to eliminate the oscillations in the vicinity of shock waves but has a very pronounced adverse impact on solution in the smooth region. This is mainly due to the fact that any TVD/MUSCL type limiters tend to degenerate solution accuracy when used in the smooth regions of the solution. Convergence history for these two solutions is compared in Fig. 12, where one can see that convergence to machine zero is observed using HWENO limiter, while the convergence history is stalled using Barth–Jespersen limiter after a drop of about three orders of magnitude, clearly demonstrating the excellent convergence behavior of HWENO limiter to a steady state solution.

The second computation is performed at a Mach number of 0.85, and an angle of attack  $1^\circ$ , using the DG method without any limiter, with Barth–Jespersen limiter and HWENO limiter, respectively. Fig. 13 shows the computed Mach number contours in the flow field obtained by these three methods, respectively. Figs. 14 and 15 show the pressure coefficient and entropy production on the surface of the airfoil obtained by these solutions, respectively. The convergence history for these solutions is compared in Fig. 16, where

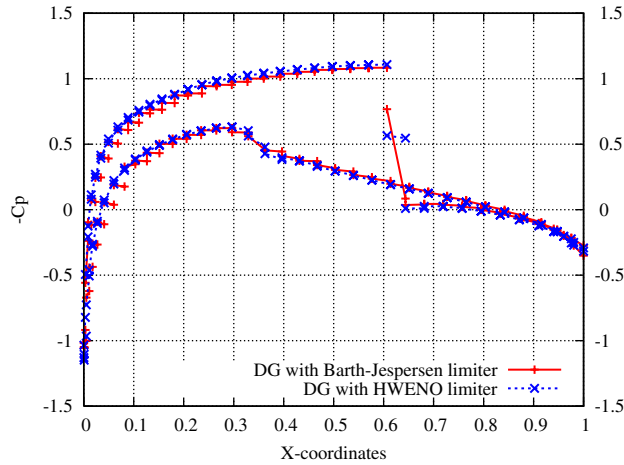


Fig. 10. Comparison of computed pressure coefficient distributions on the surface of the airfoil obtained by the DG solutions with Barth–Jespersen and HWENO limiters for transonic flow past a NACA0012 airfoil at  $M_\infty = 0.8$ ,  $\alpha = 1.25^\circ$ .

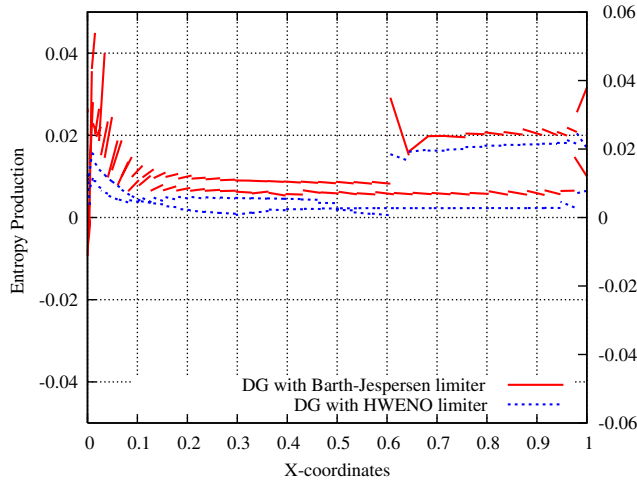


Fig. 11. Comparison of computed entropy production distributions on the surface of the airfoil obtained by the DG solutions with Barth–Jespersen and HWENO limiters for transonic flow past a NACA0012 airfoil at  $M_\infty = 0.8$ ,  $\alpha = 1.25^\circ$ .

convergence to machine zero is again observed using HWENO limiter, while convergence history is stagnant using Barth–Jespersen limiter after a drop of about three order of magnitude.

### 5.3. Transonic flow past a RAE 2822 airfoil

The third test case is the transonic flow past a RAE2822 airfoil at a Mach number of 0.73, and an angle of attack  $2.8^\circ$ . The mesh used in the computation, which consists of 2582 elements, 1360 points, and 138 boundary points, is depicted in Fig. 17. The numerical experiments are performed using DG method with Barth–Jespersen limiter and HWENO limiter, respectively. Figs. 18 and 19 show the computed Mach number contours in the flow field obtained by these two methods, respectively. The computed pressure coefficients obtained by these two computations are compared with the experimental measurement in Fig. 20. The entropy production on the surface of the airfoil obtained by these two solutions is shown in Fig. 21. Fig. 22 displays a comparison of convergence histories obtained by these two solutions, where convergence to machine zero is again observed using HWENO limiter. The superiority of the HWENO limiter over the TVD/MUSCL limiter is again demonstrated in this test case in terms of both solution accuracy and convergence performance.



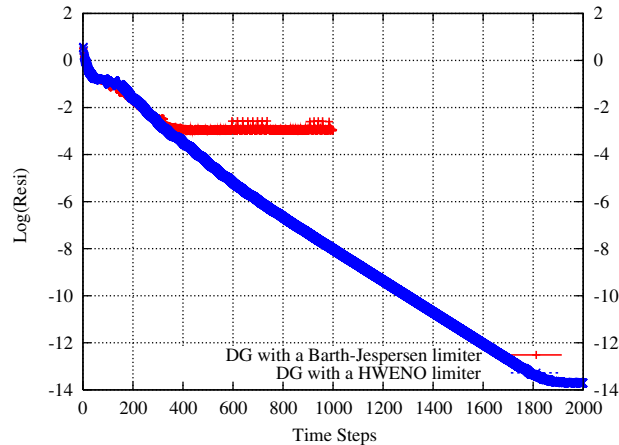


Fig. 12. Convergence history versus time steps by the DG with HWENO limiter for transonic flow past a NACA0012 airfoil at  $M_\infty = 0.8$ ,  $\alpha = 1.25^\circ$ .

#### 5.4. Supersonic flow past a wedge

The supersonic flow at  $M_\infty = 3$  past a  $15^\circ$  wedge is considered in this example. This test case is chosen to assess the ability of HWENO limiter in terms of solution accuracy and convergence performance for compute supersonic flows. The mesh used in the computation, which contains 4734 elements, 2646 points, and 192 boundary points, is depicted in Fig. 23. The computed Mach number contours in the flow field are shown in Fig. 24. To see the resolution of the oblique shock, density distribution along a horizontal line at a distance of 0.3625 from the bottom is compared with the analytical solution in Fig. 25, where the oblique shock is captured sharply without any oscillations. The convergence history for DG solutions with HWENO limiter and Barth–Jespersen limiter is displayed in Fig. 26, where convergence to machine zero is again observed for this test case, demonstrating the excellent convergence of the HWENO limiter for supersonic flows.

#### 5.5. Transonic flows past a ONERA M6 wing

A transonic flow over the ONERA M6 wing geometry is considered in this test case. The M6 wing has a leading edge sweep angle of  $30^\circ$ , an aspect of 3.8, and a taper ratio of 0.562. The airfoil section of the wing is the ONERA “D” airfoil, which is a 10% maximum thickness-to-chord ratio conventional section. The flow solutions are presented at a Mach number of 0.84 and an angle of attack of  $3.06^\circ$  using the FV method without any limiter and DG method with Barth–Jespersen and HWENO limiters. The mesh, shown in Fig. 27, contains 136,705 elements, 25,616 points, and 5017 boundary points. Fig. 28 displays the computed the Mach number contours on the upper wing surface obtained by these solutions, respectively. The upper surface contours clearly show the sharply captured lambda-type shock structure formed by the two inboard shock waves, which merge together near 80% semi-span to form the single strong shock wave in the outboard region of the wing. The computed pressure coefficient distributions are compared with experimental data at six spanwise stations in Fig. 29. The results obtained by the HWENO limiter compare closely with experimental data, except at the root stations, due to lack of viscous effects, while the other two solutions have the difficulty to capture the suction peak at the leading edge due to a lack of mesh resolution for the FV method and a use of Barth–Jespersen limiter for the DG method, which completely destroys high-order accuracy offered by the DG method. Quantitative comparison of the entropy production shown in Fig. 30 clearly conforms the accuracy of the HWENO limiter. Note that the entropy production corresponds directly to the error of the numerical methods, as it should be zero everywhere with exception of shock waves where it should increase.

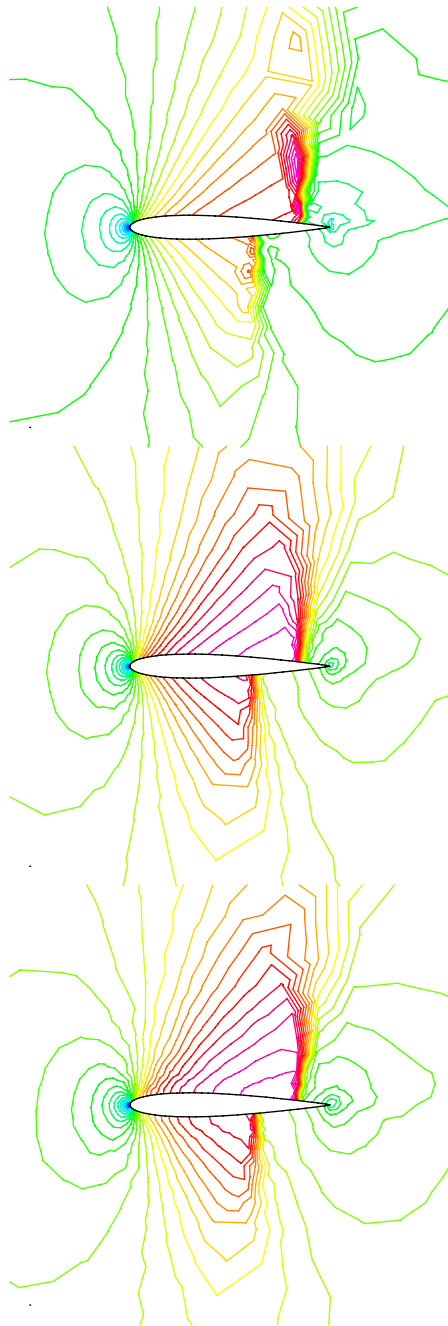


Fig. 13. Computed Mach number contours by the DG method without any limiter (top), the DG method with a HWENO limiter (middle), and the DG method with a Barth–Jespersen limiter (bottom) for transonic flow past a NACA0012 airfoil at  $M_\infty = 0.85$ ,  $\alpha = 1^\circ$ .

### 5.6. Transonic flows past a Boeing 747 aircraft

Finally, an illustrative example is presented to demonstrate that the developed method can be applied to problems of scientific and industrial interests. The computation is performed on a complete Boeing 747 aircraft using the DG method with HWENO limiter. The 747 configuration includes the fuselage, the wing, horizontal and vertical tails, underwing pylons, and flow-through engine nacelle. The mesh, used in the

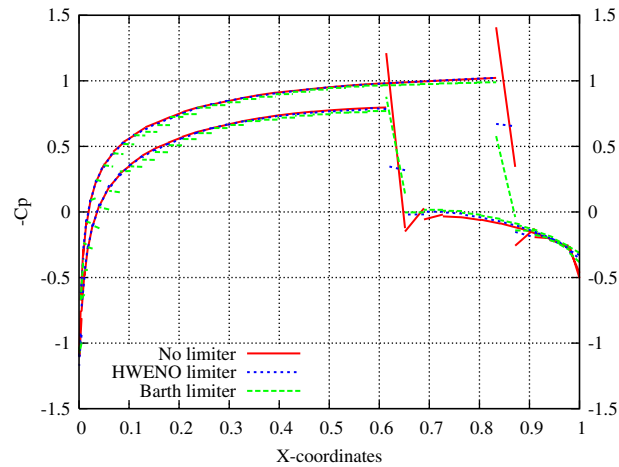


Fig. 14. Comparison of computed pressure coefficient distributions on the surface of the airfoil obtained by the DG solutions without any limiter and with Barth–Jespersen and HWENO limiters for transonic flow past a NACA0012 airfoil at  $M_\infty = 0.85$ ,  $\alpha = 1^\circ$ .

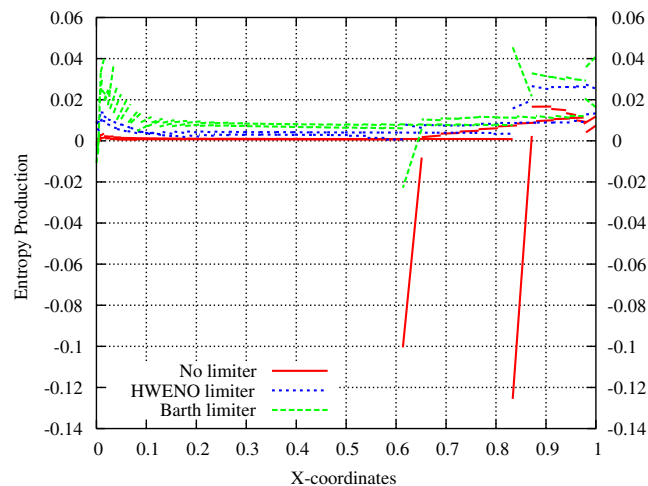


Fig. 15. Comparison of computed entropy production distributions on the surface of the airfoil obtained by the DG solutions without any limiter and with Barth–Jespersen and HWENO limiters for transonic flow past a NACA0012 airfoil at  $M_\infty = 0.85$ ,  $\alpha = 1^\circ$ .

computation, contains 91,911 grid points, 489,376 elements and 18,261 boundary points for the half-span airplane. Solution is computed for the aircraft at a free stream of Mach number of 0.84 and an angle of attack of  $2.73^\circ$ . The computed Mach number contours on the surface of the airplane, along with the surface mesh, are shown in Fig. 31. For such a level of grid resolution, the shock waves are captured well, thus confirming the accuracy and robustness of the HWENO limiter for computing complicated flows of practical importance.

### 5.7. A Mach 3 wind tunnel with a step

The test case is a classical example for testing the accuracy of numerical schemes for computing unsteady shock waves. The problem under consideration is a Mach 3 flow in a wind tunnel with a step. The tunnel is 1 length unit high and 3 length units long. The step is 0.2 length units high and is located at 0.6 length units from the left-hand end of the tunnel. The boundary conditions are that of a reflecting surface along the walls of the

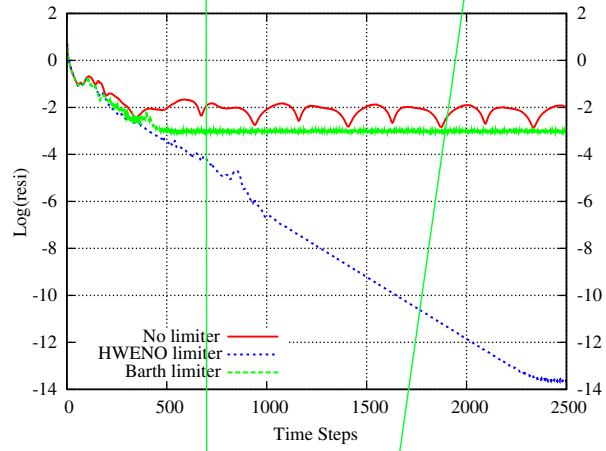


Fig. 16. Convergence history for the DG solutions without any limiter and with HWENO and Barth–Jespersen limiters for transonic flow past a NACA0012 airfoil at  $M_\infty = 0.85$ ,  $\alpha = 1^\circ$ .

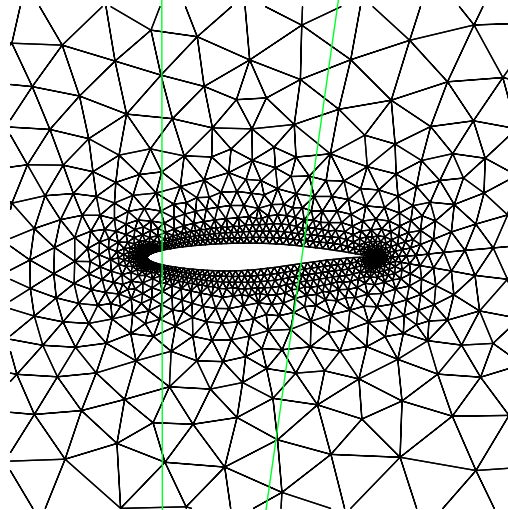
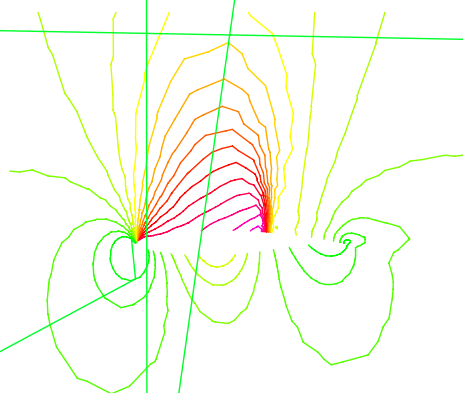


Fig. 17. Unstructured mesh ( $n_{\text{elem}} = 2582$ ,  $n_{\text{poin}} = 1360$ ,  $n_{\text{boun}} = 138$ ) used for computing transonic flow past a RAE2822 airfoil.



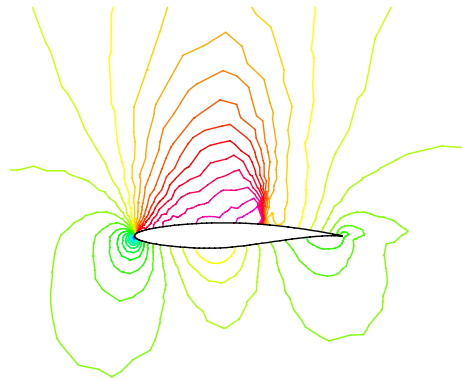


Fig. 19. Computed Mach number contours by the DG method with a Barth–Jespersen limiter for transonic flow past a RAE2822 airfoil at  $M_\infty = 0.73$ ,  $\alpha = 2.8^\circ$ .

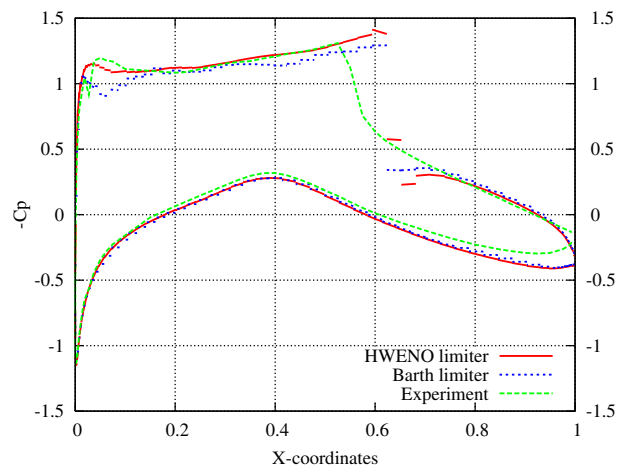


Fig. 20. Comparison of computed pressure coefficient distributions on the surface of airfoil obtained by the DG solutions with Barth–Jespersen and HWENO limiters with experimental data for transonic flow past a RAE2822 airfoil at  $M_\infty = 0.73$ ,  $\alpha = 2.8^\circ$ .

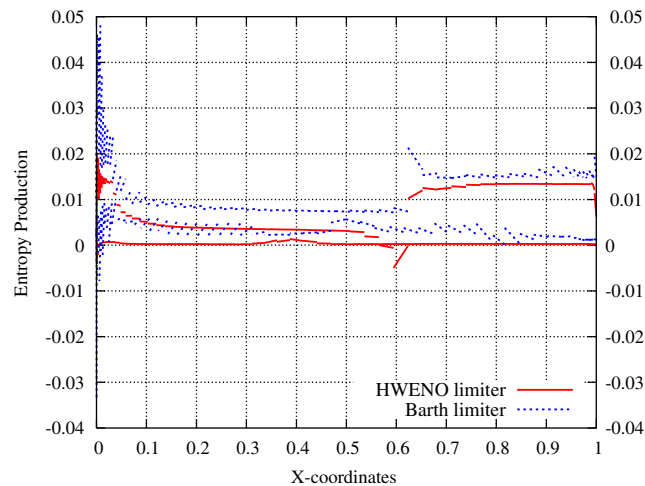


Fig. 21. Comparison of computed entropy production distributions on the surface of the airfoil obtained by the DG solutions with Barth–Jespersen and HWENO limiters for transonic flow past a RAE2822 airfoil at  $M_\infty = 0.73$ ,  $\alpha = 2.8^\circ$ .

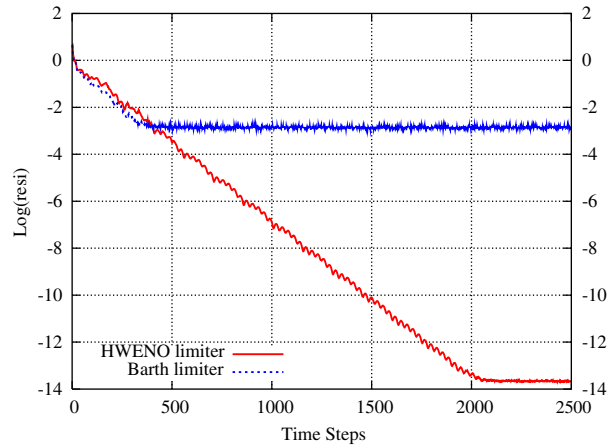


Fig. 22. Convergence history for the DG solutions with HWENO and Barth–Jespersen limiters for transonic flow past a RAE2822 airfoil at  $M_\infty = 0.73$ ,  $\alpha = 2.8^\circ$ .

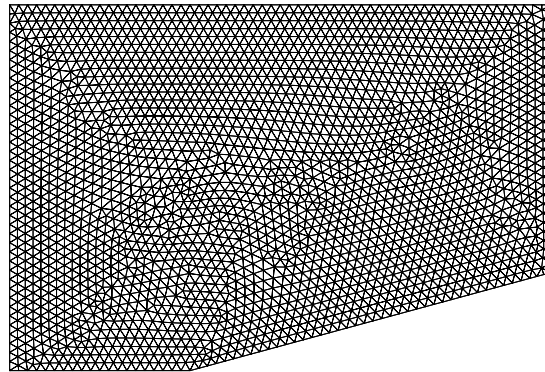


Fig. 23. Unstructured mesh ( $n_{\text{elem}} = 4734$ ,  $n_{\text{poin}} = 2464$ ,  $n_{\text{boun}} = 192$ ) used for computing supersonic flow past a wedge.

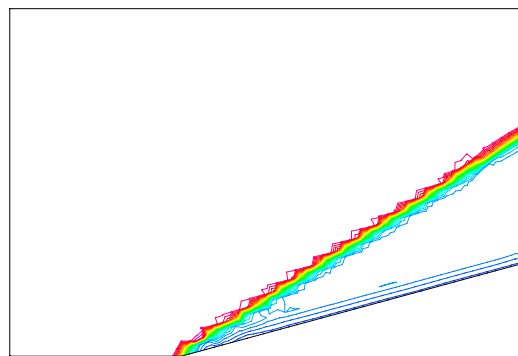


Fig. 24. Computed Mach number contours by the DG method with a HWENO limiter for supersonic flow past a wedge at  $M_\infty = 3$ .

tunnel, and characteristic boundary conditions are used at the inlet and exit. The initial condition is the uniform flow, where  $(\rho, u, v, p) = (1.4, 3, 0, 1)$ . The numerical experiment is performed on a coarse grid, which has about the same mesh size as that used in Ref. [13], where an element size of 0.025 is used everywhere else while an element size of one-quarter of that, i.e., 0.00625 is used in the corner. The resulting mesh has 10,245 elements, 5294 grid points, and 341 boundary points. Figs. 32–34 show the mesh used in the computation, the



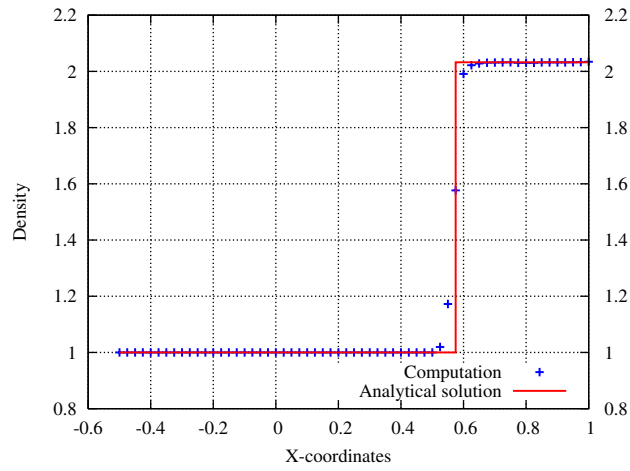


Fig. 25. Comparison of computed density distributions obtained by the DG solutions with HWENO limiter with the analytical solution along  $y = 0.3625$  for supersonic flow past a wedge at  $M_\infty = 3$ .

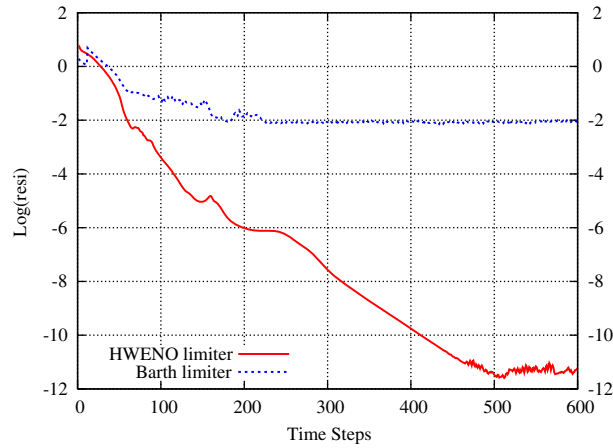


Fig. 26. Convergence history of DG solution with HWENO limiter for supersonic flow past a wedge at  $M_\infty = 3$ .

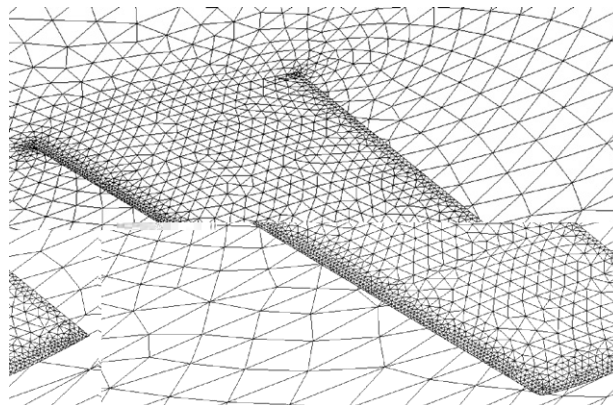


Fig. 27. unstructured surface mesh ( $n_{\text{elem}} = 136,705$ ,  $n_{\text{poin}} = 25,616$ ,  $n_{\text{boun}} = 5017$ ) used for computing transonic flow past an ONERA M6 wing.

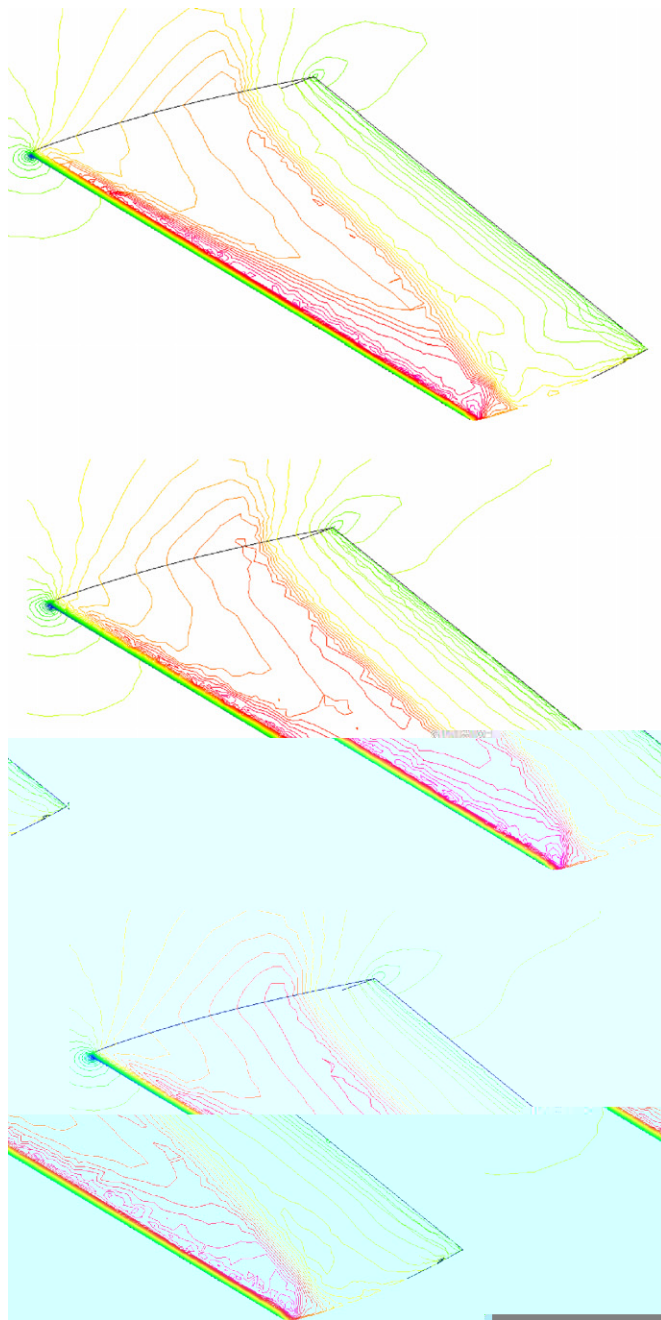


Fig. 28. Computed Mach number contours obtained by the DG methods with HWENO limiter (top) and with Barth–Jespersen limiter (middle), and the FV method without any limiter (bottom) for transonic flow past an ONERA M6 wing at  $M_\infty = 0.84$ ,  $\alpha = 3.06^\circ$ .

computed density number contours obtained by the DG method and a third-order WENO method [13], respectively. Note that 30 lines are plotted from 0.32 to 6.15 for both density contours. One can see that the shock resolution of the third-order WENO scheme is slightly more diffusive than the present second DG scheme, and the slip line coming from the lambda shock is also more visible in the second DG solution than third-order WENO solution, qualitatively demonstrating that the present second-order DG solution is as accurate as, if not more accurate than, the third-order WENO solution.

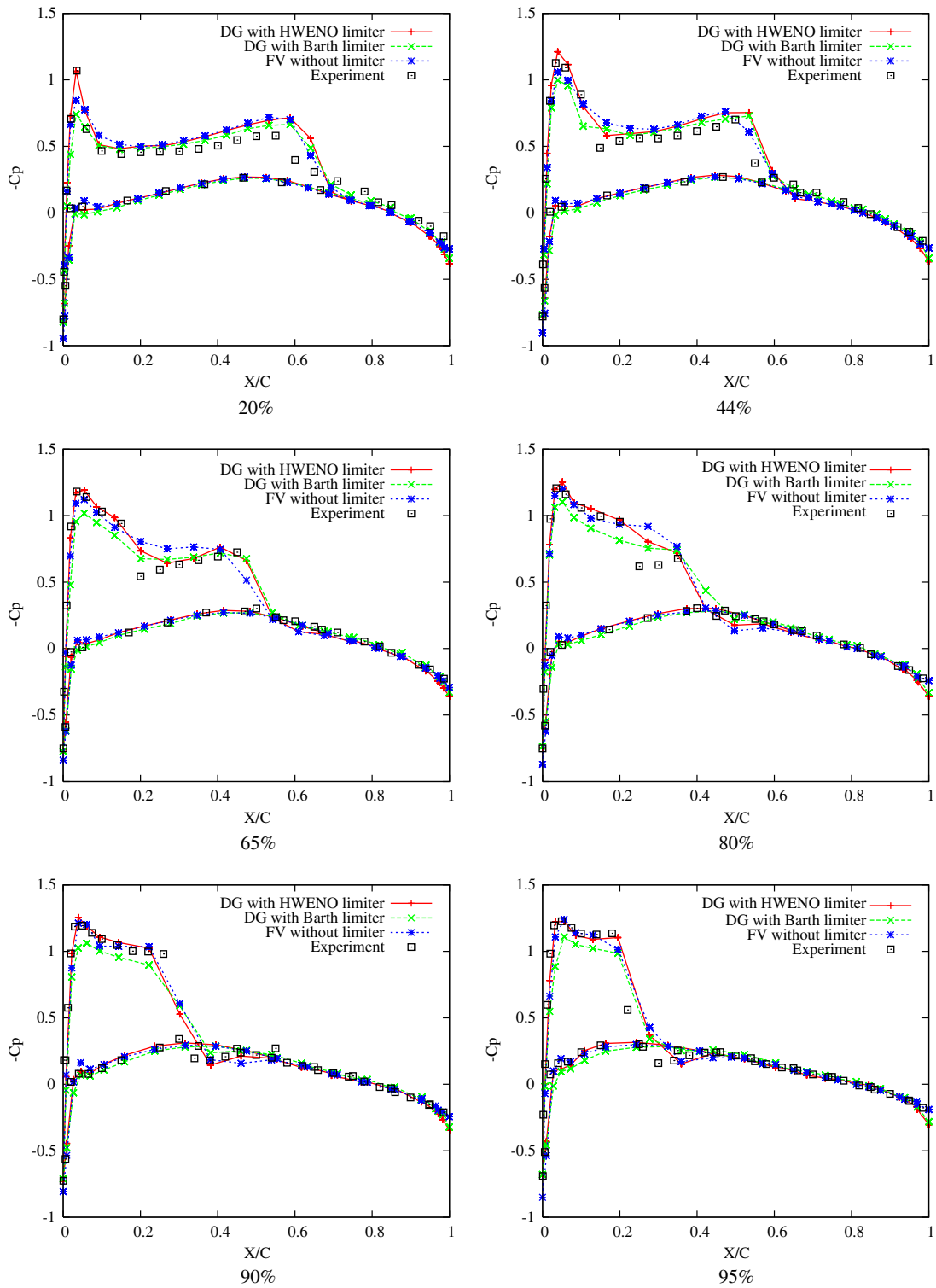


Fig. 29. Comparison of computed pressure coefficient distributions for wing section at different semispan locations obtained by the DG solutions with Barth–Jespersen and HWENO limiters and FV solution without any limiter with experimental data for transonic flow past an ONERA wing at  $M_\infty = 0.84$ ,  $\alpha = 3.06^\circ$ .

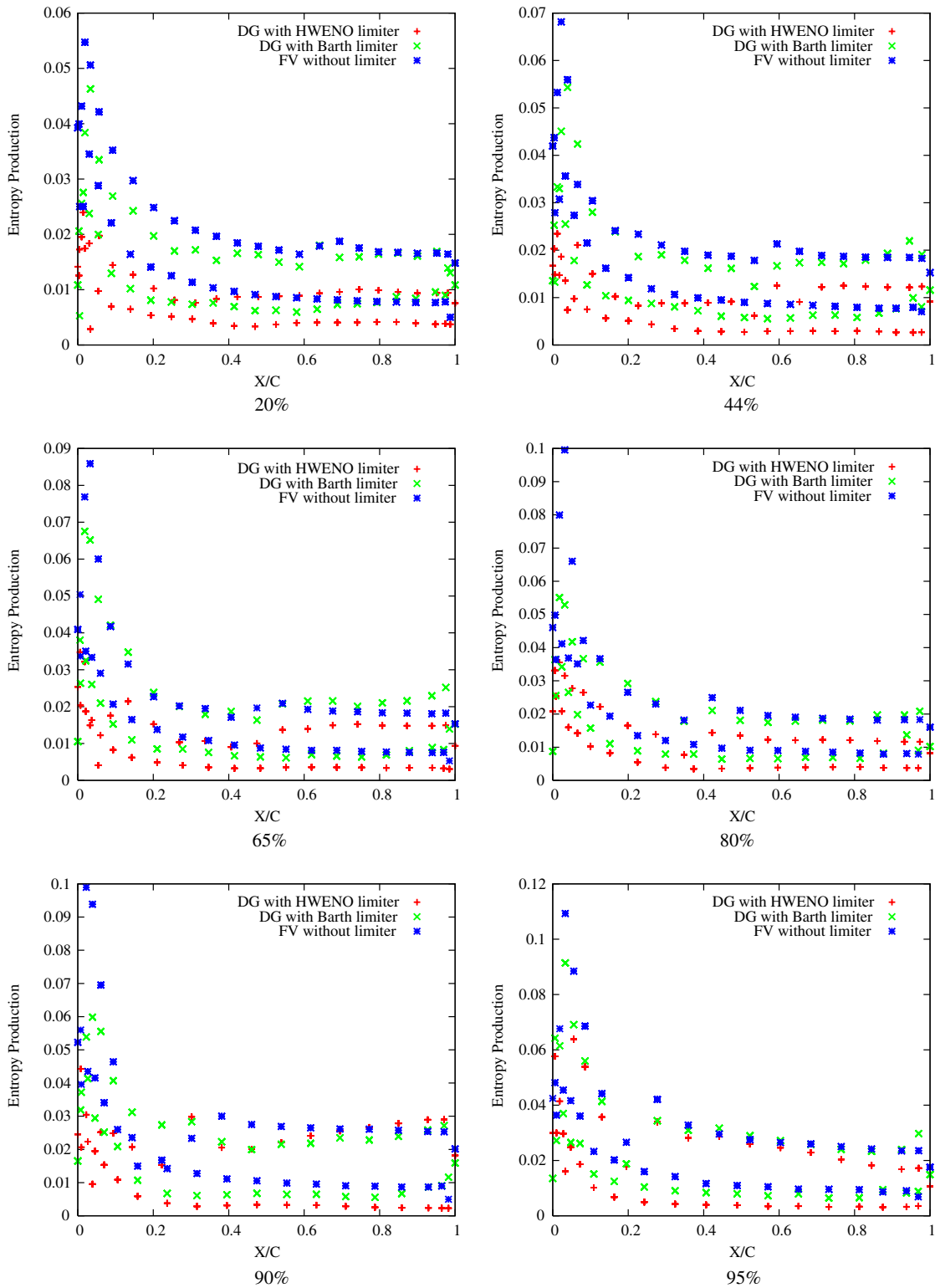


Fig. 30. Comparison of computed entropy production distributions for wing section at different semispan locations obtained by the DG solutions with Barth–Jespersen and HWENO limiters and FV solution without any limiter with experimental data for transonic flow past an ONERA wing at  $M_\infty = 0.84$ ,  $\alpha = 3.06^\circ$ .

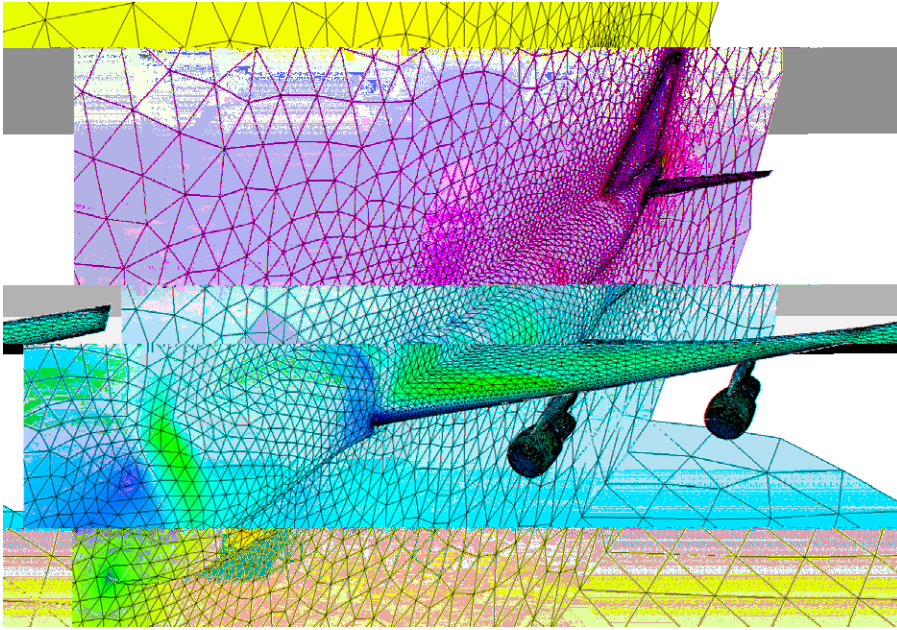


Fig. 31. Computed Mach number contours and unstructured surface mesh for transonic flow past a complete B747 aircraft ( $n_{\text{elem}} = 489,376$ ,  $n_{\text{poin}} = 91,911$ ,  $n_{\text{boun}} = 18,261$ ).

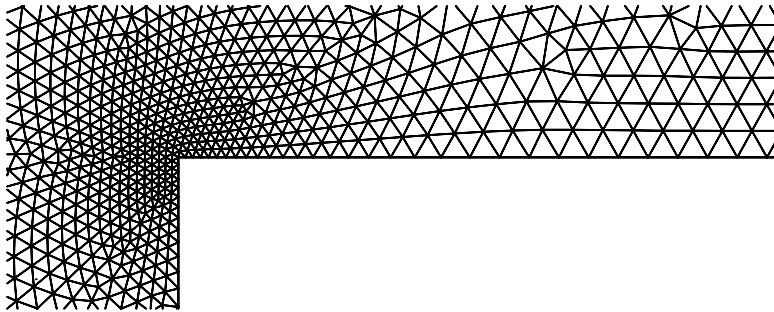


Fig. 32. Unstructured mesh ( $n_{\text{elem}} = 10,245$ ,  $n_{\text{poin}} = 5294$ ,  $n_{\text{boun}} = 341$ ) used for computing supersonic flow in a wind tunnel with a step at  $M_{\infty} = 3$ .

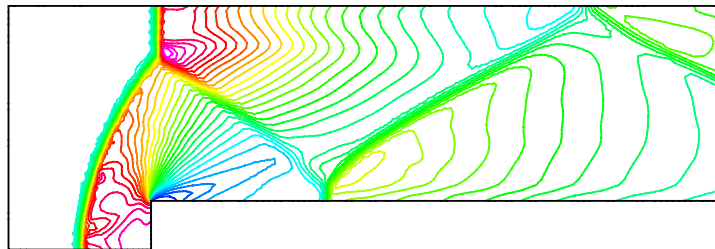


Fig. 33. Computed density contours by the present second-order DG method with the HWENO limiter for supersonic flow in a wind tunnel with a step at  $M_{\infty} = 3$ .

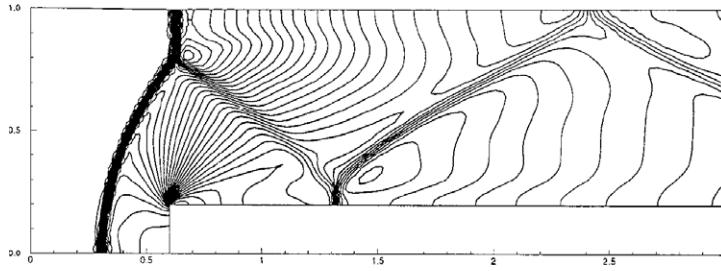


Fig. 34. Computed density contours by a third-order WENO method for supersonic flow in a wind tunnel with a step at  $M_\infty = 3$ .

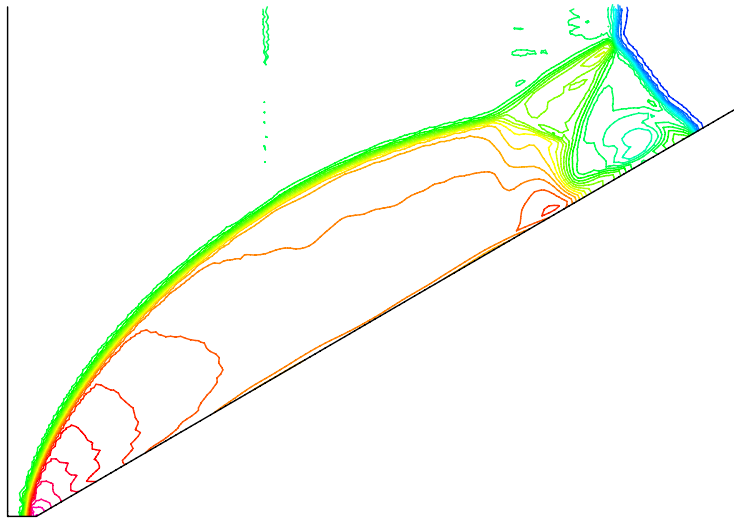


Fig. 35. Computed density contours by the second DG method with the HWENO limiter for double Mach reflection of strong shock  $M_s = 10$ .

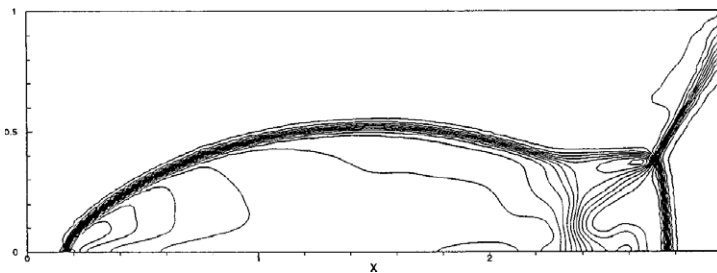


Fig. 36. Computed density contours by a third-order WENO method for double Mach reflection of strong shock  $M_s = 10$ .

### 5.8. Double mach reflection of a strong shock wave

In this case, an incident shock  $M_s = 10$  past a  $30^\circ$  wedge, a well known test case, is computed using a uniform mesh size of 0.02, the coarse grid resolution used in Ref. [13]. Figs. 35–37 show the computed density number contours obtained by the present second-order DG method, a third-order WENO method and a fourth-order WENO method [13], respectively. Thirty equally spaced lines are plotted from 1.5 to 21.5 for all density contours. One can see that the second-order DG solution is clearly better than the third-order WENO solution, and actually comparable to the fourth-order WENO solution, qualitatively demonstrating the superior accuracy of the DG method due to the HWENO limiter.



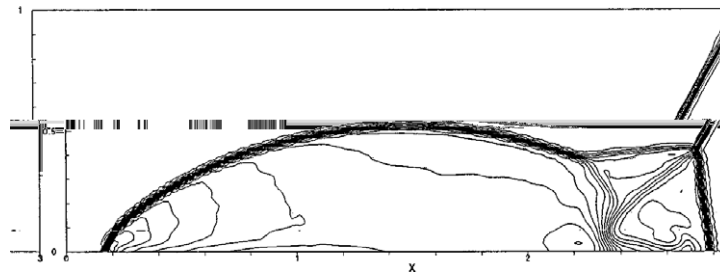


Fig. 37. Computed density contours by a fourth-order WENO method for double Mach reflection of strong shock  $M_s = 10$ .

## 6. Concluding remarks

A weighted essential non-oscillatory reconstruction scheme based on Hermite polynomials is developed and applied as a limiter for the discontinuous Galerkin finite element method on unstructured grids. The HWENO reconstruction algorithm uses the invaluable derivative information, that are handily available in the context of discontinuous Galerkin methods, thus only requires the van Neumann neighborhood for the construction of stencils. This significantly facilitates the implementation of WENO schemes on unstructured grids and greatly reduces the computational costs associated with the WENO methods. The developed HWENO limiter has been used to compute a variety of compressible flow problems for a wide range of flow conditions in both 2D and 3D configurations. The superior robustness of the HWENO limiter for the DG methods is demonstrated in terms of both solution accuracy and convergence performance in comparison with TVD/MUSCL type limiters. Using this HWENO limiter, the accuracy of the second-order DG solutions is comparable to, if not better than, that of the third-order WENO solutions using the same mesh resolution.

## Acknowledgments

The first author expresses appreciation to Prof. Shu at Brown University and Prof. Cockburn at University of Minnesota for many helpful, instructive, and fruitful discussions about DG and WENO.

## References

- [1] B. Cockburn, C.W. Shu, The Runge–Kutta discontinuous Galerkin method for conservation laws V: multidimensional system, *Journal of Computational Physics* 141 (1998) 199–224.
- [2] B. Cockburn, G. Karniadakis, C.W. Shu, The development of discontinuous Galerkin method, in: B. Cockburn, G.E. Karniadakis, C.W. Shu (Eds.), *Discontinuous Galerkin Methods, Theory, Computation, and Applications*, Lecture Notes in Computational Science and Engineering, vol. 11, Springer, New York, 2000, pp. 5–50.
- [3] H. Luo, J.D. Baum, R. Löhner, On the computation of steady-state compressible flows using a discontinuous Galerkin method, in: *Proceedings of the Fourth International Conference on Computational Fluid Dynamics*, Ghent, Belgium, 10–14, July, 2006.
- [4] A. Harden, B. Engquist, S. Osher, S.R. Chakravarthy, Uniformly high-order accurate essential non-oscillatory schemes III, *Journal of Computational Physics* 71 (1987) 231–303.
- [5] X. Liu, S. Osher, T.F. Chen, Weighted essential non-oscillatory schemes, *Journal of Computational Physics* 115 (1994) 200–212.
- [6] J. Qiu, C.W. Shu, Runge–Kutta discontinuous Galerkin method using WENO limiters, *SIAM Journal of Scientific Computing* 26 (2005) 907–929.
- [7] J. Qiu, C.W. Shu, Hermite WENO schemes and their application as limiters for Runge–Kutta discontinuous Galerkin method: one dimensional case, *Journal of Computational Physics* 193 (2004) 115–135.
- [8] J. Qiu, C.W. Shu, Hermite WENO schemes and their application as limiters for Runge–Kutta discontinuous Galerkin method II: two dimensional case, *Computers & Fluids* 34 (2005) 642–663.
- [9] A. Harden, S.R. Chakravarthy, Multidimensional ENO schemes on general geometries, ICASE Report No. 91-76, 1991.
- [10] R. Abgrall, On essential non-oscillatory schemes on unstructured meshes, *Journal of Computational Physics* 114 (1994) 45–58.
- [11] T. Sonar, On the construction of essential non-oscillatory finite volume approximation to hyperbolic conservation laws on general triangulations: polynomial recovery, accuracy, and stencil selection, *Computer Methods in Applied Mechanics and Engineering* 140 (1997) 157–182.
- [12] O. Friedrich, Weighted essential non-oscillatory schemes for the interpolation of mean values on unstructured grids, *Journal of Computational Physics* 144 (1998) 194–212.

- [13] C. Hu, C.W. Shu, Weighted essential non-oscillatory schemes on unstructured triangular meshes, *Journal of Computational Physics* 150 (1999) 97–127.
- [14] E.F. Toro, M. Spruce, W. Speares, Restoration of the contact surface in the HLL-Riemann solver, *Shock Waves* 4 (1994) 25–34.
- [15] P. Batten, M.A. Leschziner, U.C. Goldberg, Average-state Jacobians and implicit methods for compressible viscous and turbulent flows, *Journal of Computational Physics* 137 (1997) 38–78.
- [16] H. Luo, J.D. Baum, R. Löhner, High-Reynolds number viscous flow computations using an unstructured-grid method, *Journal of Aircraft* 42 (2) (2005) 483–492.
- [17] H. Luo, J.D. Baum, R. Löhner, A  $p$ -multigrid discontinuous Galerkin method for the Euler equations on unstructured grids, *Journal of Computational Physics* 211 (2) (2006) 767–783.
- [18] H. Luo, J.D. Baum, R. Löhner, A fast,  $p$ -multigrid discontinuous Galerkin method for compressible flows at all speeds, *AIAA Paper* 2006-0110, 2006.
- [19] G.S. Jiang, C.W. Shu, Efficient implementation of weighted ENO schemes, *Journal of Computational Physics* 126 (1) (1996) 202–228.
- [20] H. Luo, J.D. Baum, R. Löhner, A fast, matrix-free implicit method for compressible flows on unstructured grids, *Journal of Computational Physics* 146 (2) (1998) 664–690.
- [21] T.J. Barth, D.C. Jespersen, The design of application of upwind schemes on unstructured grids, *AIAA Paper* 1989-0366, 1989.